Subradiant Plasmon Modes in Multilayer Metal−Dielectric Nanoshells

Meng Wang, Min Cao, Xin Chen, and Ning Gu*

State Key Laboratory of Biolectronics and Jiangsu Laboratory for Biomaterials and Devices, Southeast University, Nanjing 210096, P. R. China

ABSTRACT: Subradiant plasmon modes play an important role in plasmon coupling, which can couple to the superradiant modes resulting in Fano resonances. In this study, we investigated the behaviors of the subradiant plasmons in multilayer metal−dielectric nanoshells using the generalized Mie theory. We showed that it is possible to get a pronounced Fano resonance in a single concentric nanoshell by controlling the size and geometry. The near-field coupling effects in multilayer nanoshell chains were studied by changing the alignment,

particle number, and interparticle spacing. The local electric field and induced surface charge distributions were plotted to gain physical insight into the coupling mechanisms. The interactions between the particles result in a well-developed Fano resonance due to the broadening of bright plasmon modes. The subradiant plasmon modes remain robust and nearly uninfluenced by the near-field coupling and the surrounding medium. At the Fano resonance frequency, the largest field enhancement occurs in the silica layer, which is quite different from solid metal nanoparticle chains.
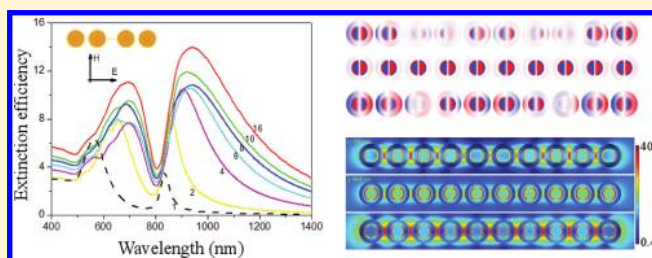
■ INTRODUCTION

Metal nanostructures have attracted considerable attention because their unique optical properties are significantly different from their bulk counterparts.[1,2] The interaction of metal nanostructures with electromagnetic radiation can result in collective excitations, known as localized surface plasmon resonance (LSPR). The frequency and intensity of LSPR depend on the composition, size, and shape of the particle as well as the refractive index of the local environment.[3−6] In nanostructures of complex geometry, such as multilayer shells, aggregates of proximal metal nanoparticles and the different plasmon modes can interact by the near-field coupling.[7,8] This provides an opportunity for designing of metallic nanostructures to manipulate light on the nanoscale by controlling the plasmonic coupling of different metallic elements.[9−11]

The physical mechanism of the plasmon coupling can be elegantly understood through the plasmon hybridization theory.[12] In complex plasmonic nanostructures, the plasmon modes can be classified as bright (superradiant) or dark (subradiant) modes. Bright modes couple to the incident light directly and are spectrally broadened due to radiative damping. Dark modes are weakly damped and spectrally narrow because they do not couple to light. When the bright mode is coupled to a dark mode, Fano resonances appear.[13] However, the plasmon hybridization theory was developed in the electrostatic limit ignoring the retardation effects. For particles of larger dimensions, more rigorous electrodynamic approaches are required. The generalized Mie theory gives an analytical solution to Maxwell's equations, which has been extended to model the light scattering by ellipsoids, cylinders, cubes, coated spheres, multispheres, etc.[14,15] Beyond Mie theory, there are various numerical methods, such as the discrete dipole approximation (DDA),[16] T-matrix approach (CTM),[17] finite difference time domain methods (FDTD),[18] and finite element

methods (FEM),[19] which have been established to calculate the optical response of arbitrarily shaped particles.[20] Although these numerical methods can also provide accurate results, it costs a much higher consumption of computational resources in numerical methods. Anyway, to study the light scattering of spherical particles or clusters, the analytical methods are relatively fast and accurate.

Recently, metal−dielectric multilayer nanoshells (MNSs) on the sub-100 nm scale have been successfully synthesized, which exhibit novel optical properties.[21,22] The optical properties of MNSs have been investigated in the literatures.[22−25] Specifically, Au@SiO$_2$@Au (gold-core/silica-shell/gold-outer-shell) MNSs can support Fano resonances due to the interaction of the subradiant and superradiant modes.[26] However, much work on plasmonic Fano resonances was carried out on metallic arrays and asymmetrical nanostructures,[27] and the near-field coupling effects on the subradiant plasmon received little attention. In this paper, we focused on the behavior of the subradiant plasmon modes in Au@SiO$_2$@Au MNSs. We first studied how to get a pronounced Fano resonance in a single MNS. Subsequently, we investigated the near-field coupling effects in MNS chains using the generalized multiparticle Mie (GMM) theory, which has been implemented for multilayer spheres. The effects of the chain alignment, number of particles, interparticle spacing, and refractive index of the medium on the interparticle interactions were also investigated. To explore the mechanism of plasmon hybridization in nanoshell chains, the local electric field and induced surface charge distributions were plotted.

■ METHOD

Electromagnetic Scattering by an Aggregate of Spheres.
Electromagnetic scattering by an arbitrary ensemble of spheres has a complete analytical solution analogous to the Mie solution for light scattering by single spheres. The GMM method can be extended to provide a general solution to the general case of an arbitrary mixture of spherical and nonspherical chatterers.[28,29] In the GMM theory, the incident and scattered fields are expanded in vector spherical wave functions around each sphere. We can solve the partial scattered field expansion coefficients (a_{mn}, b_{mn}) by applying the boundary conditions at the surface of each particle associated with vector translation theorems. Finally, we yield the following large-scale system of linear equations

$$a^l_{mn} = a^{-l}_n p^{-l}_{mn} - a^{-l}_n \sum_{j \neq l}^{(1,L)} \sum_{\nu=1}^{N^j} \sum_{\mu=-\nu}^{\nu} (A^{jl}_{mn\mu\nu} a^j_{\mu\nu} + B^{jl}_{mn\mu\nu} b^j_{\mu\nu})$$

$$b^l_{mn} = b^{-l}_n q^{-l}_{mn} - b^{-l}_n \sum_{j \neq l}^{(1,L)} \sum_{\nu=1}^{N^j} \sum_{\mu=-\nu}^{\nu} (B^{jl}_{mn\mu\nu} a^j_{\mu\nu} + A^{jl}_{mn\mu\nu} b^j_{\mu\nu})$$

$$(1)$$

where L stands for the number of spheres, (p^{-l}_{mn} q^{-l}_{mn}) are the expansion coefficients of the incident plane wave, and ($A^{jl}_{mn\mu\nu}$, $B^{jl}_{mn\mu\nu}$) are the vector translation coefficients based on the spherical Hankel function of the first kind. If particle l is a homogeneous sphere, (a^j_n, b^j_n) are the exactly Mie scattering coefficients of the isolated component sphere.

After all the expansion coefficients are solved, the total field outside the spheres can be obtained by summing the incident fields and the scattered fields, and the total extinction cross section can be calculated by the following equation

$$\mathbf{C}_{ext} = \frac{4\pi}{k^2} \sum_{l=1}^{L} \sum_{n=1}^{N^l} \sum_{m=-n}^{n} \mathrm{Re}(p^{l*}_{mn} a^l_{mn} + q^{l*}_{mn} a^l_{mn})$$

$$(2)$$

where (p^{l*}_{mn}, q^{l*}_{mn}) are the complex conjugates of (p^l_{mn}, q^l_{mn}) and k is the wave vector modulus.

Internal Electromagnetic Fields of Aggregated Multilayer Spheres. A schematic depicting the geometry of a multilayer sphere is shown in Figure 1. Analogous to the scattered fields from each individual sphere, the electromagnetic fields inside each multilayer sphere can also be expanded in terms of the vector spherical functions[30,31]

$$\mathbf{E}^{j,l}_{int} = -\sum_{n=1}^{N^j} \sum_{m=-n}^{n} iE_{mn}[c^{j,l}_{mn}\mathbf{M}^{(1)}_{mn} + d^{j,l}_{mn}\mathbf{N}^{(1)}_{mn}) + b^{j,l}_{mn}\mathbf{M}^{(3)}_{mn} + a^{j,l}_{mn}\mathbf{N}^{(3)}_{mn}]$$

$$\mathbf{H}^{j,l}_{int} = -\frac{k^j}{\omega\mu^j} \sum_{n=1}^{N^j} \sum_{m=-n}^{n} E_{mn}[d^{j,l}_{mn}\mathbf{M}^{(1)}_{mn} + c^{j,l}_{mn}\mathbf{N}^{(1)}_{mn} + a^{j,l}_{mn}\mathbf{M}^{(3)}_{mn} + b^{j,l}_{mn}\mathbf{N}^{(3)}_{mn}]$$

$$(3)$$

where ($a^{j,l}_{mn}$, $b^{j,l}_{mn}$, $c^{j,l}_{mn}$, $d^{j,l}_{mn}$) are the lth layer internal coefficients of the jth multilayer sphere and ($\mathbf{M}_{mn}$, $\mathbf{N}_{mn}$) are the vector spherical functions. The relations between the internal coefficients ($c^{j,l}_{mn}$, $d^{j,l}_{mn}$) and the scattering coefficients (a^j_{mn}, b^j_{mn}) are[32]

$$c^{j,l}_{mn} = \frac{c^{j,l}_n}{b^{j,L+1}_n} b^j_{mn}, \quad d^{j,l}_{mn} = \frac{d^{j,l}_n}{a^{j,L+1}_n} a^j_{mn}$$

$$(4)$$

where ($c^{j,l}_n$, $d^{j,l}_n$) are the lth layer Mie internal coefficients and ($a^{j,L+1}_n$, $b^{j,L+1}_n$) are the Mie scattering coefficients of the jth multilayer sphere.
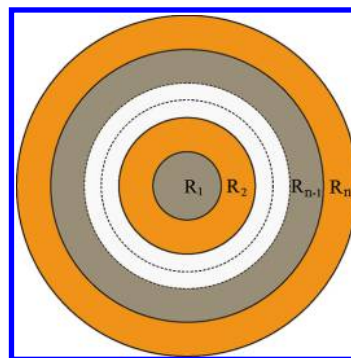

Figure 1. Schematic of a multilayered sphere.

The scattering and internal Mie coefficients ($a^{j,l}_n$, $b^{j,l}_n$, $c^{j,l}_n$, $d^{j,l}_n$) of an isolated multilayered sphere can be calculated using a recursive algorithm. Detailed descriptions of the algorithm for a single multilayer sphere can be found in several references.[30,33] The internal coefficients ($a^{j,l}_{mn}$, $b^{j,l}_{mn}$) are given by

$$a^{j,l}_{mn} = -d^{j,l}_{mn}A^{j,l}_n, b^{j,l}_{mn} = -c^{j,l}_{mn}B^{j,l}_n$$

$$(5)$$

where $A^{j,l}_n = a^{j,l}_n/d^{j,l}_n$ and $B^{j,l}_n = b^{j,l}_n/c^{j,l}_n$.[30]

Having obtained the internal coefficients of all layers, the electromagnetic fields inside each multilayer sphere can be calculated from eq 3. By applying Gauss's law to the boundary, the induced surface charge σ_p can be written as

$$\sigma_p = \varepsilon_0 \oint_s E \, ds$$

$$(6)$$

In our calculations, the MNSs are assumed to be immersed in an aqueous medium (n_{medium} = 1.33). The dielectric constant for silica is set to 2.04, and the dielectric functions for gold are taken from the data of Johnson and Christy.[34] The surface scattering should be considered when the metal thickness is smaller than the bulk mean free path.[19] However, most MNSs discussed in this paper are of the geometries that the size effects become less important and the bulk dielectric constants are adopted.

■ RESULTS AND DISCUSSION

The computer program for multilayer particles has been developed based on the GMM theory, which is able to model the near- and far-field properties of arbitrary multilayered sphere clusters. The code was verified by comparison with the FEM in terms of light scattering by a four-layered MNS dimer (Figure 2). The two MNSs, consisting of alternating gold and SiO$_2$ dielectric layers of dimension $R_1/R_2/R_3/R_4$ = 20/30/40/50 nm, align with the electric polarization with interparticle spacing d = 5 nm. FEM calculations were performed using the commercial software COMSOL Multiphysics, which allows accurate resolving of electromagnetics in nanoscale nanostructures. The far- and near-field results of the two methods are in good agreement. Three resonance peaks due to the strong near-field coupling appear in both extinction spectra. The near-field distributions almost have the same pattern, while the GMM method can provide a high-resolution pattern rapidly. The formalism is compatible with the multiple spheres with arbitrary layers; however, our studies focus on the three-layer Au@SiO$_2$@Au MNSs, which were fabricated experimentally.

Figure 3a shows the extinction spectra of Au@SiO$_2$@Au MNSs with various outer-shell thicknesses. Each spectrum has

two major peaks, which come from the coupling of dipolar plasmon modes. The extra tunability introduced by the inner gold core and silica layer provides an opportunity for controlling the strength and resonance energy of the plasmon modes of the MNSs. With the increase of the thickness of the outer shell, the low-energy resonance is blue shifted and the high-energy resonance is red shifted. It is interesting that there is a transparency region between the two dipolar resonances in the spectra, where the scattering is highly suppressed. If the shell is thick enough, the broadened dipolar resonances become very close and are separated by a sharp dip. The asymmetric line shape of this feature is analogous to the Fano resonance, which has been observed commonly in atomic physics studies. In contrast to the conventional resonance, the Fano resonance exhibits a distinctly asymmetric profile.
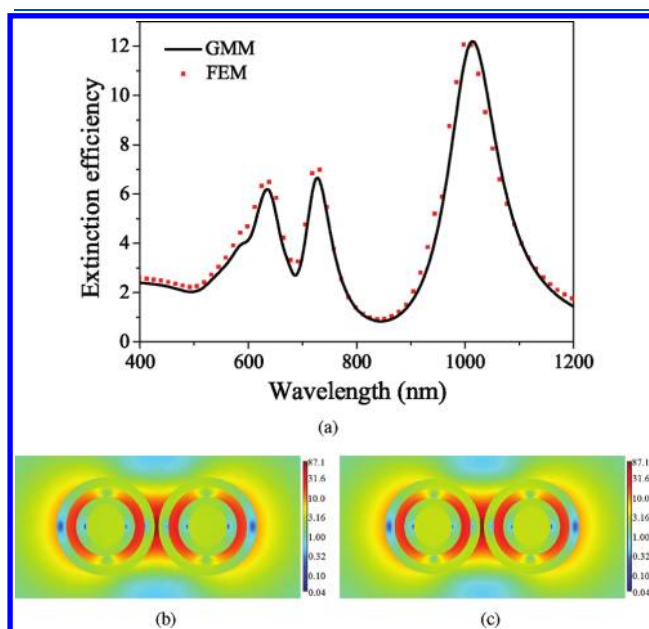
According to the plasmon hybridization theory, the two bright dipolar plasmon modes, which come from hybridization of the lower energy bonding shell plasmon mode with the inner gold core plasmon mode, dominate the optical response of the Au@SiO$_2$@Au MNSs. Additionally, there exists an antisymmetric bonding mode corresponding to a subradiant plasmon mode. This mode has a very small dipole moment leading to suppression of scattering. As is known, coupling of the superradiant with the subradiant plasmons can induce a Fano resonance in its optical response.[22] However, the appearance of the Fano resonance depends on the following aspects. First, for small-sized MNSs, the superradiant modes are not broad enough to couple with the subradiant mode. Second, if the outer shell is very thin, the bonding resonance will shift to much lower energy far from the subradiant mode. Finally, if the silica layer is very thick, the antisymmetric bonding mode will not cancel the total moment dipole effectively. To conclude, a Au@SiO$_2$@Au MNS consisting of a relatively thick gold shell and thin silica layer can exhibit a pronounced Fano resonance in the optical spectrum. Figure 3b shows the extinction efficiencies of several large-sized MNSs. For $R_1/R_2/R_3$ = 30/50/80 nm and 45/70/100 nm, the subradiant mode is red shifted to 625 and 713 nm respectively, where an apparent Fano resonance appears. For the MNS with larger size ($R70/120/150$ nm), excitation of multipolar modes greatly broadens the dipolar resonances and the subradiant mode is red shifted to 880 nm and appears as an asymmetric antiresonance. Since the subradiant plasmon modes strongly depend on the geometry of the MNS, the Fano spectral feature is difficult to obtain in experiments due to the heterogeneity in nanoparticle size.

Let us now consider the effect of the near-field coupling in MNS chains. Figure 4 shows the extinction efficiencies for a chain of $R25/30/50$ nm Au@SiO$_2$@Au MNSs with various numbers of particles (N = 2, 4, 6, 8, 10). For the case of perpendicular alignment as shown in Figure 4a, from a single MNS to a MNS dimer, the higher energy dipolar plasmon red shifts and the lower energy plasmon blue shifts distinctly. As the number of MNS increases, the two dipolar plasmons shift very little. For the case of parallel alignment as shown in Figure 4b, the two bright dipolar plasmons are greatly broadened and shift to lower energy with the increase of particle number. However, this red shift does not follow a monotonic trend which was also reported by Wei et al.[35] The resonance peak wavelength for N = 10 is blue shifted relative to the spectrum for N = 8. More multipolar plasmon resonance peaks appear as weak shoulders in spectra for N = 2, 4, 6 at shorter
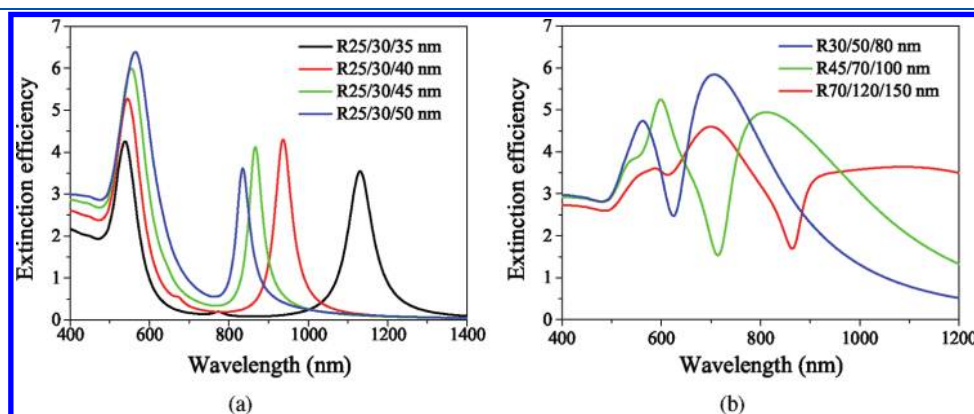

Figure 2. Comparison of the calculated extinction and near-field results of GMM theory and FEM. (a) Extinction efficiency of a $R20/30/40/50$ nm Au@SiO$_2$@Au@SiO$_2$ MNS dimer with interparticle spacing of 5 nm. Local electric fields in the $x-y$ plane plotted in logarithmic scale calculated from FEM (b) and GMM theory (c) at the dipolar resonance wavelength (λ = 1010 nm).

Figure 3. (a) Extinction efficiencies of Au@SiO$_2$Au MNSs with various outer-shell thicknesses. (b) Extinction efficiencies of large-sized Au@SiO$_2$Au MNSs.

20922

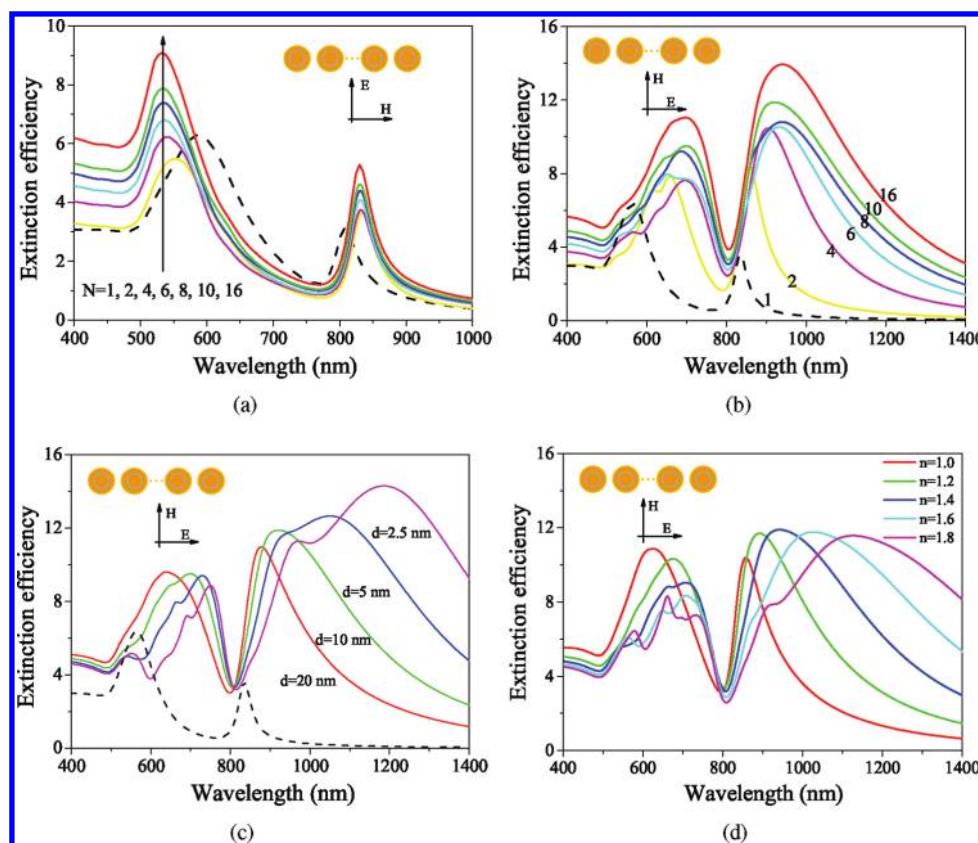dx.doi.org/10.1021/jp205736d |*J. Phys. Chem. C* 2011, 115, 20920–20925

Figure 4. Extinction efficiencies of $R25/30/50$ nm Au@SiO$_2$@Au MNS chains. MNSs aligned normal (a) and parallel (b) to the polarization with different particle numbers ($d = 10$ nm). (C) MNSs aligned parallel to the polarization with different spacings ($N = 10$). (d) MNS chain embedded in mediums with different refractive indices ($N = 10$, $d = 10$ nm). The dashed line corresponds to a single Au@SiO$_2$@Au MNS.

wavelengths. When the particle number is larger than 8, these resonance peaks vanish in the broadened dipolar resonances. The dip in the extinction spectra is sharpened by the broadened dipolar resonance peaks with a little shift from 780 to 810 nm, where a well-developed Fano resonance is formed. The effects of the interparticle spacing are shown in Figure 4c. The decreasing separations also result in a red shift and broadening of the dipolar plasmon modes due to the multipolar plasmon modes coupling. For the smaller spacing, the bonding dipolar mode moves to longer wavelength rapidly because the near-field coupling strength is proportional to d^{-3}. However, in all cases, the strong near-field coupling has little effect on the subradiant plasmon mode.

In many applications, the Fano resonance is found to be sensitive to the surrounding medium. By employing subradiant plasmon modes in LSPR sensing, a high figure of merit (FOM) can be achieved. Therefore, we investigate the effect of the surrounding medium on the optical properties of the MNS chain. As shown in Figure 4d, when the medium refractive index is increased from 1.0 to 1.8, the superradiant plasmon modes continuously red shift and broaden significantly and there is a little red shift in the Fano resonance (from 795 to 807 nm). The spectral shifts are similar to that induced by the decrease in the interparticle space. Let us give a quantitative interpretation of the results; on one hand, the subradiant mode of the MNS depends more on the inner geometry than the total size; on the other hand, increasing the refractive index of the surrounding medium is equivalent to enlarging the particle size spatially, which results in a smaller gap spacing. It suggests that the subradiant plasmon is inherent in the MNS geometry,

which offers an opportunity for designing active plasmonic devices, such as optical switches and modulators.

These results are qualitatively similar to what has previously been studied for solid nanoparticle chains.[7] In closely spaced particle chains, the near-field couplings between the nearby particles dominate the behavior of plasmon resonances which can be described as a chain of point dipoles interacting via their near fields. The interparticle coupling will lead to shifts in the frequency of the plasmon resonance due to the change of the restoring force acting on the oscillating electrons of the particles.[1] However, for MNS aggregates, the near-field coupling is affected not only by the interparticle distance but also by the geometry of the MNS. The extinction, absorption, and scattering spectra are plotted, respectively, for a silica−gold−silica MNS chain ($R_1/R_2/R_3 = 25/30/50$ nm, $N = 10$, $d = 10$ nm) as shown in Figure 5a. The results show that the scattering efficiency is much larger than the absorption efficiency in most wavelength bands, indicating that radiative damping is the dominant decay mechanism. At the wavelength nearby the subradiant plasmon resonance peak ($\lambda = 808$ nm), the scattering is suppressed highly and an absorption peak appears, which means that the subradiant mode acquires strength from the superradiant mode and releases energy through nonradiative damping. It is quite different from the solid particle case (dashed line in Figure 5a), whose scattering dominates the whole extinction spectrum.

The associated surface charge distributions can help us to explore the plasmonic coupling mechanism in MNS chains. Figure 5b shows the induced surface charge distributions of a Au@SiO$_2$@Au
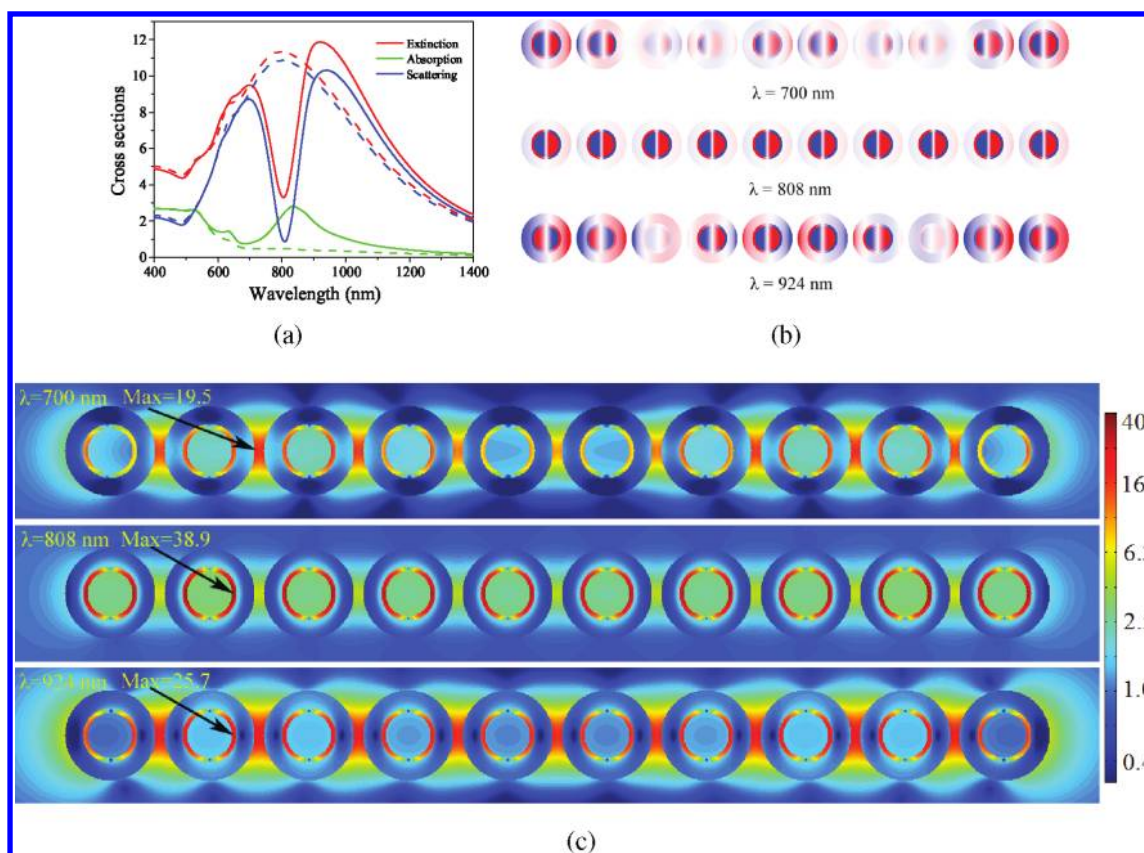
Figure 5. Far- and near-field optical properties of a $R25/30/50$ nm Au@SiO$_2$@Au MNS chain ($N = 10$, $d = 10$ nm). Optical cross sections (a), surface charge distributions (b), and electric field intensities (c) are plotted. The dashed lines in (a) correspond to a solid gold nanoparticle chain.

MNS chain ($R_1/R_2/R_3 = 25/30/50$ nm, $N = 10$) at resonance peak wavelengths. Radiative damping can be determined by the surface charge of the outer surface ($R = R_3$). It is found that the surface charges of the outer surface oscillate in different phases exhibiting complementary patterns along the chains like a standard wave. The superradiant plasmon modes ($\lambda = 700, 924$ nm) can be identified by the fractions of the surface charge wave.[36] At the Fano resonance frequency ($\lambda = 808$ nm), the surface charges of the outer surface of each MNS in chain are very weak, resulting in suppression of radiative damping. The surface charges of the cavity ($R = R_2$) and the gold core ($R = R_1$) always oscillate out of phase, which provides the restoring force driving the plasmon oscillations.

The electric field distributions are examined as shown in Figure 5c. The points of the maximum field enhancement ($|E_{max}/E_0|$) are also marked in the figure. The surface charge distributions are directly related to the strength of the local field. The results show that the electric fields are strongly localized in the silica layer and the gap between the particles and the field intensities in the gold core of the shell are very weak and almost homogeneous. For the bright plasmon modes ($\lambda = 700, 924$ nm), intense electric fields occur in the gap region and silica layer alternatively. However, for the dark mode ($\lambda = 808$ nm), there are weak field enhancements in the scattered field leading to induced transparency, while the electric field highly concentrates in the silica layer. It is understandable that the field intensities across the gaps and silica layers also show complementary patterns due to the wave behavior of the surface charge. The maximal field enhancement $|E_{max}/E_0| = 38.9$ occurs in the silica layer at the Fano resonance wavelength. These results are quite

different from those of a solid gold nanoparticle chain, whose maximal field enhancement always occurs in the gap between the particles at the dipolar plasmon resonance wavelength. As we calculated (data not shown), a solid gold nanoparticle chain ($R = 50$ nm, $d = 10$ nm) has maximum field enhancement $|E_{max}/E_0| = 23.5$ at $\lambda = 796$ nm, which is much smaller than the MNS chains.

■ **CONCLUSION**

In summary, a formalism based on the GMM theory has been constructed for modeling the optical properties of MNS aggregates. The results reveal that an individual Au@SiO$_2$@Au MNS with proper configuration can exhibit a pronounced Fano resonance due to the coupling between the bright and the dark dipolar plasmon. As the studies extend to MNS chains, the superradiant plasmons are red shifted and more multipolar plasmons participate in the coupling broadening the superradiant modes. It is worth noting that the near-field coupling and the surrounding medium have little effect on the dark plasmon mode. The interactions between the broadened superradiant and subradiant plasmons particles result in a well-developed Fano resonance. Moreover, at the Fano resonance frequency, the corresponding electric field intensity in the silica layer is strongest due to suppression of scattering. It is anticipated that this feature of the subradiant plasmons will lead to an efficient energy transfer through the chain waveguide, and the analogous phenomenon will be observable in more complex nanostructures. We hope this study can give rise to versatile applications, including noninvasive optical detection,

20924

dx.doi.org/10.1021/jp205736d |*J. Phys. Chem. C* 2011, 115, 20920–20925

design of active optical devices, and surface-enhanced Raman scattering.

■ AUTHOR INFORMATION

Corresponding Author
*E-mail: guning@seu.edu.cn.

■ REFERENCES

(1) In *Plasmonics: Fundamentals and Applications*; Maier, S. A., Ed.; Springer: New York, 2006.

(2) In *Optical Properties of Metal Clusters*; Kreibig, U., Vollmer, M., Eds.; Springer: New York, 1995.

(3) Kelly, K. L.; Coronado, E.; Zhao, L. L.; Schatz, G. C. *J. Phys. Chem. B* **2003**, *107*, 668–677.

(4) Xia, Y.; Xiong, Y. J.; Lim, B.; Skrabalak, S. E. *Angew. Chem., Int. Ed.* **2009**, *48*, 60–103.

(5) Liz-Marzan, L. M. *Langmuir* **2006**, *22*, 32–41.

(6) Cao, M.; Wang, M.; Gu, N. *J. Phys. Chem. C* **2009**, *113*, 1217–1221.

(7) Chern, R. L.; Liu, X. X.; Chang, C. C. *Phys. Rev. E* **2007**, *76*, 016609.

(8) Khlebtsov, B.; Zharov, V.; Melnikov, A.; Tuchin, V.; Khlebtsov, N. *Nanotechnology* **2006**, *17*, 5167–5179.

(9) Halas, N. J.; Lal, S.; Chang, W.-S.; Link, S.; Nordlander, P. *Chem. Rev.* **2011**, *111*, 3913–3961.

(10) Fan, J. A.; Wu, C. H.; Bao, K.; Bao, J. M.; Bardhan, R.; Halas, N. J.; Manoharan, V. N.; Nordlander, P.; Shvets, G.; Capasso, F. *Science* **2010**, *328*, 1135–1138.

(11) Anker, J. N.; Hall, W. P.; Lyandres, O.; Shah, N. C.; Zhao, J.; Van Duyne, R. P. *Nat. Mater.* **2008**, *7*, 442–453.

(12) Prodan, E.; Radloff, C.; Halas, N. J.; Nordlander, P. *Science* **2003**, *302*, 419–422.

(13) Miroshnichenko, A. E.; Flach, S.; Kivshar, Y. S. *Rev. Mod. Phys.* **2010**, *82*, 2257–2298.

(14) In *Absorption and Scattering of Light by Small Particles*; Bohren, C. F., Huffman, D. R., Eds.; Wiley: New York, 1983.

(15) In *Scattering, Absorption, and Emission of Light by Small Particles*; Mishchenko, M. I., Travis, L. D., Lacis, A. A., Eds.; Cambridge University Press: Cambridge, 2002.

(16) Draine, B. T.; Flatau, P. J. *J. Opt. Soc. Am. A* **1994**, *11*, 1491–1499.

(17) Mishchenko, M. I.; Travis, L. D. *J. Quant. Spectrosc. Radiat. Transfer* **1998**, *60*, 309–324.

(18) In *Computational Electrodynamics: The Finite-Difference Time-Domain Method*; Taflove, A., Ed.; Artech House: Boston, MA, London, 1995.

(19) Khoury, C. G.; Norton, S. J.; Vo-Dinh, T. *ACS Nano* **2009**, *3*, 2776–2788.

(20) In *Optical Properties of Nanoparticle Systems: Mie and Beyond*; Quinten, M., Ed.; Wiley-VCH: Weinheim, 2011.

(21) Xia, X. H.; Liu, Y.; Backman, V.; Ameer, G. A. *Nanotechnology* **2006**, *17*, 5435–5440.

(22) Bardhan, R.; Mukherjee, S.; Mirin, N. A.; Levit, S. D.; Nordlander, P.; Halas, N. J. *J. Phys. Chem. C* **2010**, *114*, 7378–7383.

(23) Radloff, C.; Halas, N. J. *Nano Lett.* **2004**, *4*, 1323–1327.

(24) Hu, Y.; Fleming, R. C.; Drezek, R. A. *Opt. Express* **2008**, *16*, 19579–19591.

(25) Kodali, A. K.; Schulmerich, M. V.; Palekar, R.; Llora, X.; Bhargava, R. *Opt. Express* **2010**, *18*, 23302–23313.

(26) Mukherjee, S.; Sobhani, H.; Lassiter, J. B.; Bardhan, R.; Nordlander, P.; Halas, N. J. *Nano Lett.* **2010**, *10*, 2694–2701.

(27) Luk'yanchuk, B.; Zheludev, N. I.; Maier, S. A.; Halas, N. J.; Nordlander, P.; Giessen, H.; Chong, C. T. *Nat. Mater.* **2010**, *9*, 707–715.

(28) Xu, Y. L. *Appl. Opt.* **1995**, *34*, 4573–4588.

(29) Xu, Y. L. *Phys. Rev. E* **2003**, *67*, 046620.

(30) Yang, W. *Appl. Opt.* **2003**, *42*, 1710–1720.

(31) Liu, C. H.; Li, B. Q. *J. Phys. Chem. C* **2011**, *115*, 5323–5333.

(32) Xu, Y. L.; Gustafson, B. A. S.; Giovane, F.; Blum, J.; Tehranian, S. *Phys. Rev. E* **1999**, *60*, 2347–2365.

(33) Wu, Z. S.; Wang, Y. P. *Radio Sci.* **1991**, *26*, 1393–1401.

(34) Johnson, P. B.; Christy, R. W. *Phys. Rev. B* **1972**, *6*, 4370–4379.

(35) Wei, Q. H.; Su, K. H.; Durant, S.; Zhang, X. *Nano Lett.* **2004**, *4*, 1067–1071.

(36) Willingham, B.; Link, S. *Opt. Express* **2011**, *19*, 6450–6461.

20925

dx.doi.org/10.1021/jp205736d |*J. Phys. Chem. C* 2011, 115, 20920–20925